

RESULTS FROM BRAHMS EXPERIMENT AT RHIC*

PAWEL STASZEL

for the BRAHMS Collaboration

I.G. BEARDEN^g, D. BEAVIS^a, C. BESLIU^j, Y. BLYAKHMAN^f
 B. BUDICK^f, H. BØGGILD^g, C. CHASMAN^a, C.H. CHRISTENSEN^g
 P. CHRISTIANSEN^g, J. CIBOR^c, R. DEBBE^a, E. ENGER^l
 J.J. GAARDHØJE^g, K. HAGEL^h, O. HANSEN^g, A. HOLM^g, A.K. HOLME^l
 H. ITO^k, E. JAKOBSEN^g, A. JIPA^j, J.I. JØRDREⁱ, F. JUNDT^b
 C.E. JØRGENSEN^g, R. KARABOWICZ^d, T. KEUTGEN^h, E.J. KIM^a
 T. KOZIK^d, T.M. LARSEN^l, J.H. LEE^a, Y.K. LEE^e, G. LØVHØIDEN^l
 Z. MAJKA^d, A. MAKEEV^h, B. MCBREEN^a, M. MIKELSEN^l
 M. MURRAY^h, J. NATOWITZ^h, B.S. NIELSEN^g, J. NORRIS^k
 K. OLCZANSKI^a, J. OLNES^a, D. OUERDANE^g, R. PLANETA^d, F. RAMI^b
 C. RISTEA^j, D. RÖHRICHⁱ, B.H. SAMSET^l, D. SANDBERG^g
 S.J. SANDERS^k, R.A. SHEETZ^a, P. STASZEL^g, T.F. THORSTEINSEN^{i†}
 T.S. TVETER^l, F. VIDEBÆK^a, R. WADA^h, A. WIELOCH^d
 AND I.S. ZGURA^j

^aBrookhaven National Laboratory, Upton, New York 11973, USA^bInstitut de Recherches Subatomiques
and Université Louis Pasteur, Strasbourg, France^cInstitute of Nuclear Physics, Kraków, Poland^dJagiellonian University, Kraków, Poland^eJohns Hopkins University, Baltimore, Maryland 21218, USA^fNew York University, New York, New York 10003, USA^gNiels Bohr Institute, University of Copenhagen, Denmark^hTexas A&M University, College Station, Texas 77843, USAⁱUniversity of Bergen, Department of Physics, Bergen, Norway^jUniversity of Bucharest, Romania^kUniversity of Kansas, Lawrence, Kansas 66049, USA^lUniversity of Oslo, Department of Physics, Oslo, Norway*(Received April 11, 2002)*

* Presented at the Cracow Epiphany Conference on Quarks and Gluons in Extreme Conditions, Cracow, Poland, January 3-6, 2002.

† Deceased

We present the results from the BRAHMS experiment at the Relativistic Heavy Ion Collider (RHIC) for the $^{197}\text{Au}+^{197}\text{Au}$ reaction at $\sqrt{s_{NN}} = 130$ GeV and $\sqrt{s_{NN}} = 200$ GeV. The main focus is here on the determination of the pseudorapidity distribution of charged particles produced in the reaction as a function of pseudorapidity and centrality and on the measurement of the anti-proton to proton ratio as a function of rapidity. Our measurements show that up to 3860 and 4630 charged particles are produced in the top 5% central collisions and that the number of produced particles per participating nucleon pair exceeds values from $p+p$ collisions by about 40% and 50% for $\sqrt{s_{NN}} = 130$ GeV and $\sqrt{s_{NN}} = 200$ GeV, respectively. The $N(\bar{p})/N(p)$ ratio at mid-rapidity is found to be 0.64 ± 0.06 for the lower, and around 0.75 for the top RHIC energy. These values are the highest observed so far in nucleus–nucleus reaction and show a tendency for matter and antimatter to balance at mid-rapidity as the bombarding energy increases, they also indicate that the net-baryon free mid-rapidity plateau (Bjorken limit) is not reached at this RHIC energies. It is also shown that current models are not able to consistently describe the particle multiplicities and the baryonic ratios.

PACS numbers: 25.75.-q, 25.75.Dw

1. Introduction

In late August 2000 the Relativistic Heavy Ion Collider, RHIC, began colliding Au beams, each at an energy of 65 GeV per nucleon. In mid-August 2001 a systematic data collecting by the 4 RHIC experiment, namely BRAHMS, PHENIX, PHOBOS and STAR, began at the energy of $\sqrt{s_{NN}} = 200$ GeV. The RHIC operation started a new era of systematic studies of strongly interacting matter created in ultra-relativistic nucleus–nucleus collisions. These studies will eventually lead to a quantitative understanding of “bulk QCD”.

Multiplicity distribution and anti-particle to particle ratios of produced charged particles provide a fundamental measure of the ultra-relativistic reactions. The particle densities are sensitive to the relative contribution of “soft” processes, involving the longer length scales associated with non-perturbative QCD mechanisms, and “hard”, partonic processes [1,2]. The total number of charged particles and the angular dependence of the charged particles distribution is expected to depend markedly on the amount of hadronic rescattering, the degree of chemical and thermal equilibrium, and the role of subnucleonic processes.

The anti-particle to particle ratios are of importance in the study of matter–antimatter balance since they provide the relative abundance of anti-particles produced, therefore, give some hints about the reaction dynamics which is related to the degree of transparency achieved. Two collision scenarios are strictly related to the anti-baryon to baryon ratios (*e.g.* \bar{p}/p): the full-stopping scenario, where all the baryons participating in the reaction were transported from the beam rapidity to mid-rapidity [3,4], and the full transparency scenario, where the mid-rapidity zone was free from the partons originating from colliding nucleons [5].

2. BRAHMS experiment

BRAHMS (**B**road **R**ange **H**adron **M**agnetic **S**pectrometers), consists of two magnetic spectrometers, which allow for the determination of charged particle properties over a wide rapidity, transverse momentum range, and a number of global detectors used to characterize the general features of the reaction, such as the overall charged particle multiplicity and the flux of spectator neutrons at very forward angles. A perspective view of the experimental setup is presented in figure 1 and a detail description of the BRAHMS experimental setup can be found in [6].

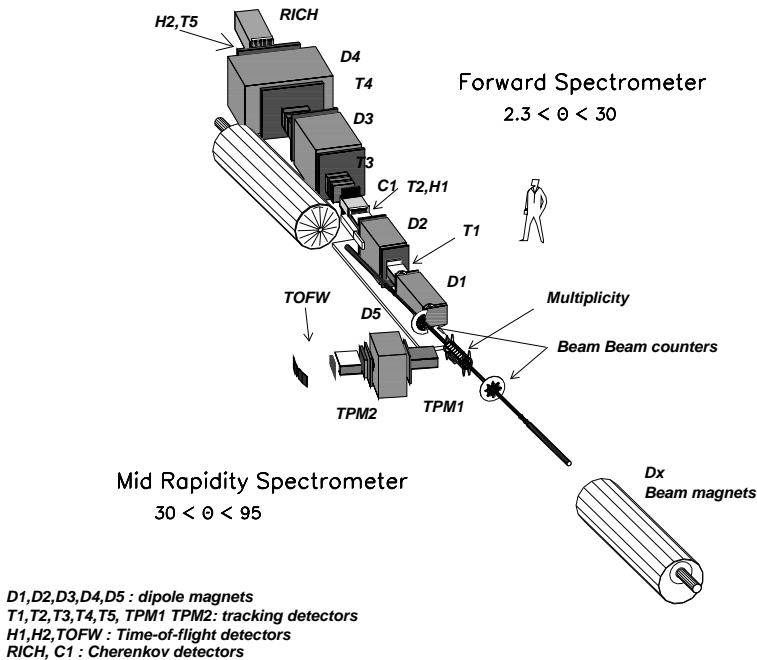


Fig. 1. The BRAHMS experiment setup in perspective.

3. Charge particle multiplicity

The charge particle multiplicities were studied using global detectors, including the Multiplicity Array (MA), the Beam–Beam Counter arrays (BBC), and the Zero-Degree Calorimeters (ZDC), as well as the front time-projection chamber (TPM1) of the MRS.

3.1. Global detectors

The Multiplicity Array consists of two independent systems, a silicon strip detector array (SiMA) surrounded by an outer array of plastic scintillator tile detectors (TMA) in a double, hexagonal-side barrel arrangement. Each of the Si detectors ($4\text{ cm} \times 6\text{ cm} \times 300\text{ }\mu\text{m}$) is located 5.3 cm from the beam axis and is subdivided along the beam direction into seven active strips. The TMA has 35 plastic-scintillator tiles ($12\text{ cm} \times 12\text{ cm} \times 0.5\text{ cm}$) located 13.9 cm from the beam axis. The effective pseudorapidity coverage of the MA is $-3 \leq \eta \leq 3$. Particle multiplicities are deduced from the observed energy loss in the SiMA and TMA element, and the elements are calibrated using low-multiplicity events, where well defined peaks corresponding to single-particle hits are observed [6, 7].

The BBC arrays are located 220 cm from the nominal interaction point. Each counter consist of two sets of Cherenkov radiators coupled to the photomultiplier tubes. The primary task of the BBC is to provide a level 0 trigger and a start time for particle time of flight measurements. The time resolution of the BBC elements allows us to determine the interaction point with an accuracy better than 0.9 cm. Charged particle multiplicities within $2.1 \leq \eta \leq 4.7$ are deduced from the number of particles hitting each detector, as found by dividing the measured detector signal by that corresponding to a single particle hitting the detector.

The ZDC detectors are located $\pm 18\text{ m}$ from the nominal interaction point and measure neutrons that are emitted at small angles with respect to the beam direction [8]. Clean selection of minimum-biased events required a coincidence between the two ZDC detectors and a minimum of 4 “hits” in the TMA. Such selection includes 95% of the Au + Au total inelastic cross section. There are identical sets of ZDCs in all of the RHIC experiments. This makes possible a cross check of the results from all four experiments and provides luminosity measurements for the RHIC machine group.

In general, statistical errors on the measurements are less than 1%, with systematic errors of 8% and 10% for the SiMA and BBC arrays, respectively. However, the systematic errors are dominated by uncertainties resulting from the calibration procedures and should lead to a common scale offset for data obtained at different RHIC energies.

3.2. Reaction centrality

The centrality selection for the experiment was deduced from a minimum-biased multiplicity distribution using the MA, assuming that a cut on the total multiplicity translates to a cut on collision centrality. Figure 2 shows the multiplicity distribution of charged particles established by the MA, normalized to the maximum observed multiplicity. The independent multiplicity measurements of the SiMA and TMA detectors are summed for this figure, after the SiMA multiplicity was rescaled to account for the difference in the geometric coverage of the two arrays.

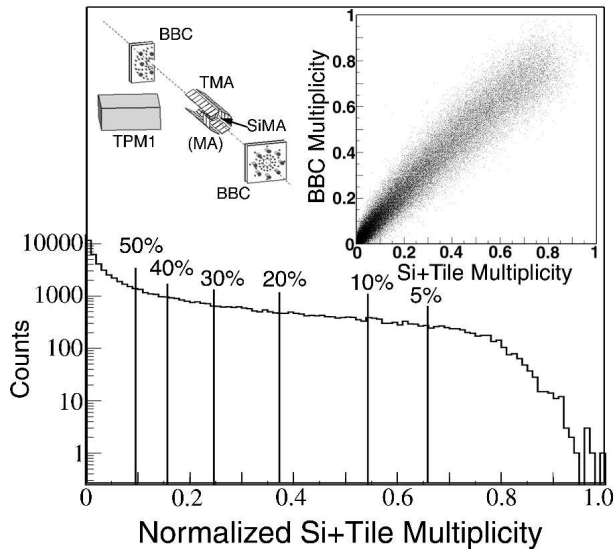


Fig. 2. Normalized MA array multiplicity distribution, as discussed in the text. The scatter plot insert shows the correlation of the normalized BBC and MA multiplicities. A schematic drawing of the global detectors used in the measurement, excluding the ZDCs, is also shown.

3.3. Results

The pseudorapidity distribution of emitted charged particles, $dN_{\text{ch}}/d\eta$, is a fundamental observable in ultra-relativistic collisions. Study of $dN_{\text{ch}}/d\eta$ versus η and centrality can address issues like the role of hard scatterings between partons and the interactions of these partons in a high-density environment. Because the collision centrality can be related to the number of nucleons participating in the reaction [9], different systems can be compared based on a simple nucleon–nucleon superposition models [10].

Figure 3 shows the measured $dN_{\text{ch}}/d\eta$ distributions for charged particles for several centrality regions for the $\sqrt{s_{NN}} = 130$ GeV data. Large pseudorapidity points (triangles) are obtained from BBC arrays and a middle and central rapidity from SiMA (dots) and TMA (squares). The black stars-points represent TPM1 data for 90° , 60° and 40° of the MRS settings. Within the systematic uncertainties, as pointed out in Sec. 3.1, we find a good agreement among measurements using different detection techniques. For the top 5% centrality cut we found $dN_{\text{ch}}/d\eta|_{\eta=0} = 553 \pm 1(\text{stat}) \pm 36(\text{syst})$. The integrated number of charge particles over the covered η range, for the same centrality cut, is 3860 ± 300 . The observed particle densities are about 1.8 times greater than observed for central events in Pb + Pb collisions at $\sqrt{s_{NN}} = 17.2$ GeV [7,11].

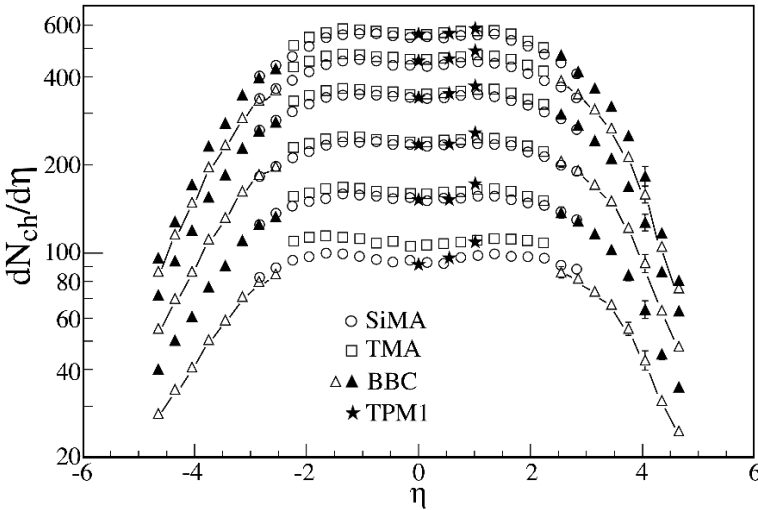


Fig. 3. Distributions of $dN_{\text{ch}}/d\eta$ for centrality ranges of, top to bottom, 0–5%, 5–10%, 10–20%, 20–30%, 30–40%, and 40–50%. Statistical uncertainties are shown, where larger than the symbol size. The connecting lines and alternating open and closed symbols for the BBC data are to help distinguish points associated with different centrality ranges.

Figure 4 shows the $dN_{\text{ch}}/d\eta$ for the maximum RHIC energy for the four selected centrality cuts indicated on the figure. The distributions were obtained by averaging the values for negative and positive pseudorapidity to further decrease the experimental uncertainties. For the most central collisions (0–5%) at $\sqrt{s_{NN}} = 200$ GeV, $dN_{\text{ch}}/d\eta|_{\eta=0} = 625 \pm 1(\text{stat}) \pm 55(\text{syst})$. This gives a scaled multiplicity value of $(dN_{\text{ch}}/d\eta)/\langle N_{\text{part}}/2 \rangle = 3.5 \pm 0.3$ charged particles per participating nucleon pair and indicates a $(11 \pm 4)\%$ increase relative to Au + Au reactions at $\sqrt{s_{NN}} = 130$ GeV [7,12]. For the

most peripheral collisions analyzed here (40–50%), we found $dN_{\text{ch}}/d\eta|_{\eta=0} = 100 \pm 10$, resulting in the scaled value of 3.0 ± 0.4 . By integrating the 0–5% multiplicity density distribution we deduced that 4630 ± 370 charged particles are emitted in the covered rapidity range. This value is $(21 \pm 4)\%$ higher than at $\sqrt{s_{NN}} = 130$ GeV [7]. For comparison we plot the predictions of Kharzeev and Levin model [13] (solid lines) which is based on a classical QCD calculations using parameters fixed to the 130 GeV data. As it is seen this approach is able to reproduce the magnitude and shape of the distributions quite well. The dashed lines are the results of AMPT model calculations [14,15], which is a cascade model based on HIJING but including final state rescattering of produced particles. This model also accounts for the general trend of the measured distributions. We also plot the similar distributions [16] from $p\bar{p}$ collisions at $\sqrt{s_{NN}} = 200$ GeV, scaled up by the corresponding number of Au + Au pairs, for the 0–5% and 40–50% centralities. For the most central collisions the Au + Au data shows a strong enhancement over the entire pseudorapidity range relative to elementary collisions. The excess is about 50% which indicates a significant medium effects in central Au + Au reactions.

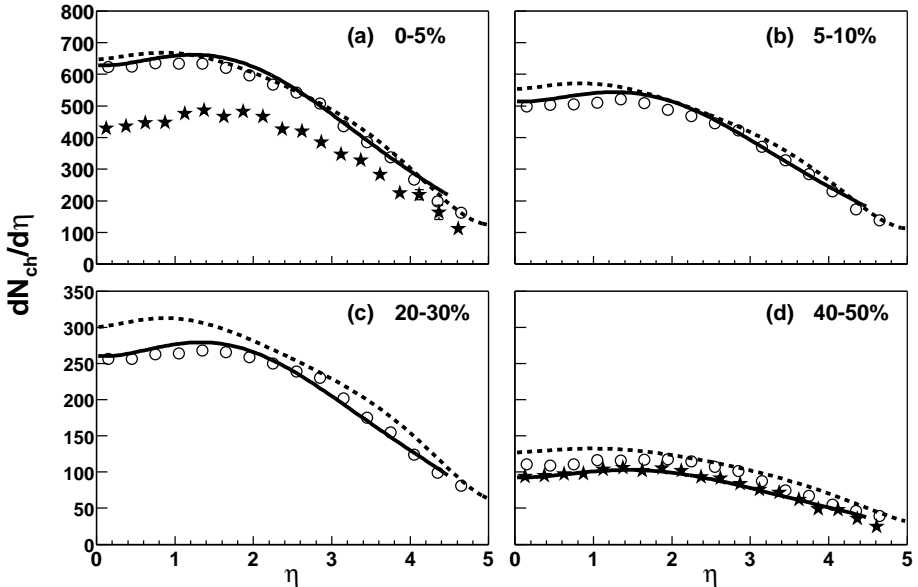


Fig. 4. Measured $dN_{\text{ch}}/d\eta$ distributions for centrality ranges of 0–5%, 5–10%, 20–30% and 40–50%. Theoretical predictions by Kharzeev and Levin (solid line) and by the AMPT model (dashed line) are also shown. Results from $p\bar{p}$ collisions at $\sqrt{s}=200$ GeV [16], scaled by the Au+Au values of $\langle N_{\text{part}} \rangle / 2$, are shown with stars ((a),(d)).

The $dN_{\text{ch}}/d\eta$ for $\sqrt{s_{NN}} = 130$ GeV (regular characters) and $\sqrt{s_{NN}} = 200$ GeV (bold characters), at selected centralities and pseudorapidities are listed in Table I, together with the average number of participating nucleons $\langle N_{\text{part}} \rangle$. The last parameter was estimated from the HIJING model [17] using default parameters.

TABLE I

$dN_{\text{ch}}/d\eta$ as a function of centrality and pseudorapidity. Total uncertainties, dominated by the systematics, are indicated. The average number of participants $\langle N_{\text{part}} \rangle$ is given for each centrality class based on HIJING model calculations. The last column gives the integral charged particle multiplicity within the pseudorapidity range $-4.7 \leq \eta \leq 4.7$.

Centrality	$\langle N_{\text{part}} \rangle$	$\eta = 0$	$\eta = 3.0$	$\eta = 4.5$	N_{ch}
0–5%	352	553±36	372±37	107±15	3860±300
	357	625±55	470±44	181±22	4630±370
5–10%	299	447±29	312±36	94±13	3180±250
	306	501±44	397±37	156±18	3810±300
10–20%	235	345±23	243±27	79±10	2470±190
	239	377±33	309±28	125±14	2920±230
20–30%	165	237±16	172±18	59±8	1720±130
	168	257±23	216±17	90±10	2020±160
30–40%	114	156±11	117±13	43±6	1160±90
	114	174±16	149±14	64±7	1380±110
40–50%	75	98±7	77±9	30±4	750±60
	73	110±10	95±9	43±5	890±70

The charged particle density $dN_{\text{ch}}/d\eta$ can be used to estimate so called Bjorken energy density, ε [5]. The formula

$$\varepsilon = \frac{3}{2} \times \frac{\langle E_{\text{T}} \rangle}{\pi R^2 \tau_0} \times \frac{dN_{\text{ch}}}{d\eta} \quad (1)$$

provides the value of ≈ 3.5 GeV/fm³ and ≈ 4 GeV/fm³ for $\sqrt{s_{NN}} = 130$ GeV and $\sqrt{s_{NN}} = 200$ GeV, respectively. In (1) we assumed that $\tau_0 = 1$ fm/c, $\langle E_{\text{T}} \rangle = 0.5$ GeV and $R = 6$ fm, for both energies. Factor 3/2 is due to the assumption that the charged particles carried out of the reaction zone take only a fraction (2/3) of the total available energy. These values are significantly above the energy density expected to result in quark–gluon plasma formation [18].

In figure 5 we plot particles densities normalized to the number of participating pairs for SPS data, RHIC data at $\sqrt{s_{NN}} = 130$ GeV, and RHIC data at $\sqrt{s_{NN}} = 200$ GeV for two selected centrality cuts. Data at different beam energies are plotted as a function of the pseudorapidity shifted by the respective beam rapidity. The figure shows that charged particle multiplicities in an interval of approximately 0.5–1.5 units below the beam rapidity are independent of the collision centrality and energy, from the CERN SPS energy ($\sqrt{s_{NN}}=17$ GeV) [11] to the present RHIC energy. This observation is consistent with a limiting fragmentation picture in which the excitation of the fragment baryons saturates already at moderate collisions energies. In contrast, what is evidenced by the observed increase of the multiplicities per participating pair around $\eta = 0$, the increased projectile kinetic energy is utilized for particle production in the region around mid-rapidity.

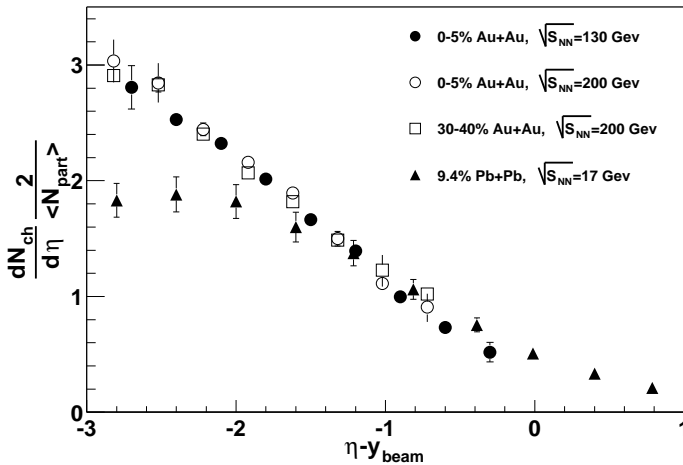


Fig. 5. Charged-particle multiplicities normalized to the number of participant nucleon pairs (see Table) for the present 0–5% central (open circles) and 40–50% central (open squares) Au+Au results at $\sqrt{s_{NN}}=200$ GeV, the BRAHMS 0–5% Au+Au results [7] at $\sqrt{s_{NN}}=130$ GeV (closed circles) and the 9.4% central Pb+Pb data at $\sqrt{s_{NN}}=17$ GeV (closed triangles) of Ref. [11]. Data at different beam energies are plotted as a function of the pseudorapidity shifted by the relevant beam rapidity. Representative total uncertainties are shown for a few Au+Au points.

The ratios of $dN_{ch}/d\eta(\eta)$ measured at $\sqrt{s_{NN}}=130$ GeV and $\sqrt{s_{NN}}=200$ GeV for different centralities are shown in figure 6. An increase in the particle density as a function of energy for the central plateau region is observed. The increase is comparable for all centralities and range between 10 and 20%. The plotted curves show the corresponding ratios resulting from the two model calculations. The upturn of the ratios at forward rapidities is due to widening of the pseudorapidity distribution at higher energy.

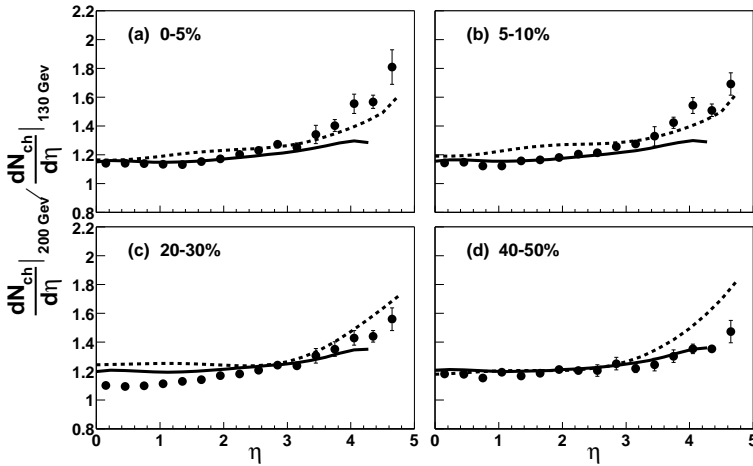


Fig. 6. Ratio of $dN_{\text{ch}}/d\eta$ values at $\sqrt{s_{NN}}=200$ GeV and 130 GeV compared to the model calculations (see figure 3 caption). Total uncertainties are shown, assuming a 3% relative scaling uncertainty between the two energies.

Finally, in figure 7 we plot $dN_{\text{ch}}/d\eta(\eta)/\langle N_{\text{part}}/2 \rangle$ as a function of the number of participants, for 3 narrow pseudorapidity regions, namely around $\eta = 0, 3$ and 4.5. It is seen that at forward rapidities the particle production per participant pair is remarkably constant and near unity, however the

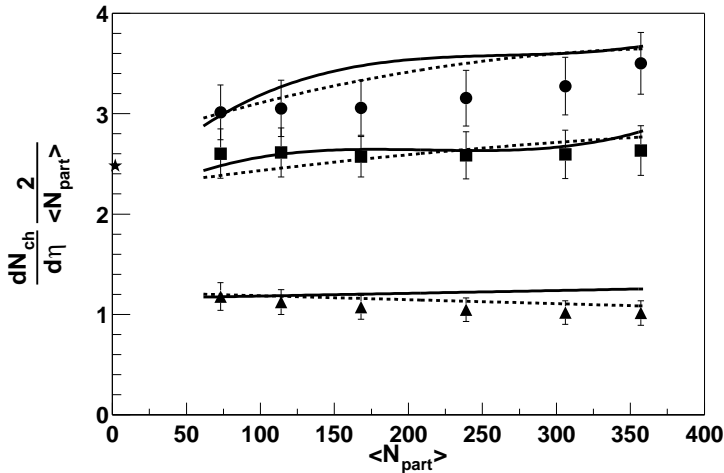


Fig. 7. $dN_{\text{ch}}/d\eta$ per participant nucleon pair as a function of the average number of participants (see Table) for $\eta = 0$ (circles), 3.0 (squares) and 4.5 (triangles). The curves show the model predictions (see figure 3 caption). The star denotes the $p\bar{p}$ result at $\eta = 0$ [16].

curve plotted for central rapidity rises as a function of collision centrality. This behavior is attributed to the onset of hard scattering which scales with N_{coll} rather than N_{part} [19–21]. Using N_{coll} values from HIJING we fit the observed dependencies to the soft–hard parameterization [22]:

$$dN_{\text{ch}}/d\eta = \alpha N_{\text{part}} + \beta N_{\text{coll}}. \quad (2)$$

For central events at $\eta \approx 0$ we found that the hard-scattering component to the charged-particle production remains almost constant, with values of $(20 \pm 7)\%$ and $(25 \pm 7)\%$ at $\sqrt{s_{NN}} = 130$ and 200 GeV, respectively.

4. Anti-particle to particle ratios

The anti-particle to particle ratios rapidity dependence give us the possibility of studying the reaction mechanism between heavy ions at high energies. It is expected that such a reaction will evolve from full stopping to complete transparency with increasing collision energy. In the case of full stopping, the partons of the colliding nuclei will be shifted from the rapidity of the incident beam to mid-rapidity ($y \approx 0$), leading to the formation of a central zone with significant net-baryon density. In the case of full transparency, also called the Bjorken limit [5], the baryons from the interacting nuclei will, after the collision, also be shifted slightly from beam rapidity, since they have lost energy but the mid-rapidity region will be devoid of original baryons. In this region, the net-baryon density is zero, but the energy density is high. Almost full stopping is observed in Au + Au reaction at AGS energies ($\sqrt{s_{NN}} = 5 \text{ GeV}$). In reactions between Pb at SPS energies, $\sqrt{s_{NN}} = 17 \text{ GeV}$, transparency begins to set in, and systematics suggest that maximum baryon density occurs at energies intermediate between AGS and SPS [4,23]. The situation of maximum baryon density and of vanishing net-baryon density at mid-rapidity give rise to entirely different initial conditions for the possible creation of a deconfined quark–gluon system.

4.1. BRAHMS spectrometer

The very different momenta and particle densities at mid-rapidity and forward angles has led to a design with two independent, movable magnetic spectrometers. The perspective view of the spectrometers layout is shown in figure 1.

The Mid-Rapidity Spectrometer (MRS), has a solid angle of 6.5 msr and consists of the single dipole magnet (D5) placed between two TPCs which are used for tracking. Particle IDentification in the MRS is based on momentum and Time-Of-Flight (TOF) measurement. In MRS the TOF is provided by six hodoscope panels positioned along a circle centered on the middle of the

magnet D5 with a radius of 2.4 meters. In figure 8 we plot distribution of the inverse particle velocity, β^{-1} , versus particle momentum. The picture shows bands representing p , \bar{p} , K^- , K^+ and π^- , π^+ , well separated in the momentum range $p < 4$ GeV/ c for kaons and protons, and up to $p = 2$ GeV/ c for pions and kaons.

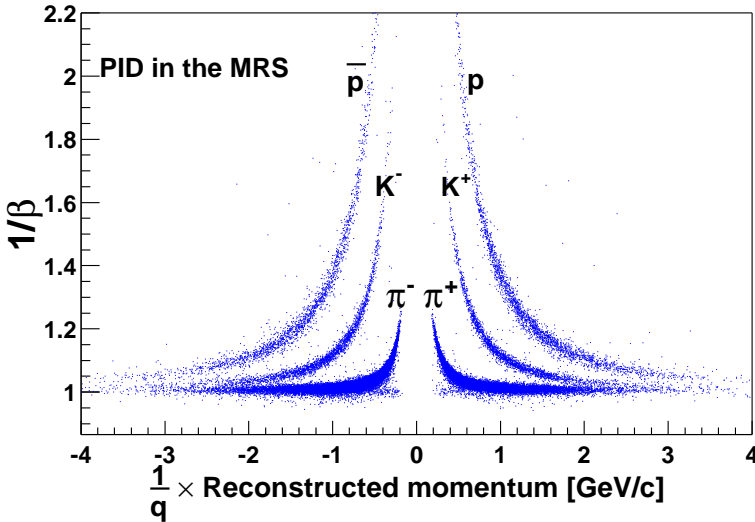


Fig. 8. Particle identification in the MRS.

The Forward Spectrometer (FS) has a solid angle of 0.8 msr and can measure and identify charged particles heaving momenta up to 25 GeV/ c in the angular range of $2.3^\circ < \theta < 30^\circ$. Four magnets (D1–D4) are used for sweeping and analyzing particles emerging from the reaction zone. The front arm of the FS tracking detectors are Time Projection Chambers (T1 and T2), which provide a good three-dimensional track recognition and background rejection in a high multiplicity environment. The back arm of the FS tracking detectors are Drift Chambers (DCs, T3–T5), each DC consists of three identical modules that contain 10 (8) detection planes for T3 (T4–T5). Like in the MRS, PID is based on momentum and TOF measurements. The FS consists of two TOF detectors, H1 and H2, placed (positioned) 9 and 20 meters from the nominal interaction point, respectively. For higher momenta, PID is obtained via a threshold Cherenkov detector (C1), placed behind D2 magnet, and a Ring Imaging Cherenkov (RICH), placed behind H2 hodoscope. Figures 9 and 10 show particle identification capabilities for H1 and RICH detector, respectively. Note that the particle momenta of the data plotted in top and bottom panel of figure 10 ranging 8 to 20 GeV/ c and 3 GeV/ c to 6 GeV/ c , respectively.

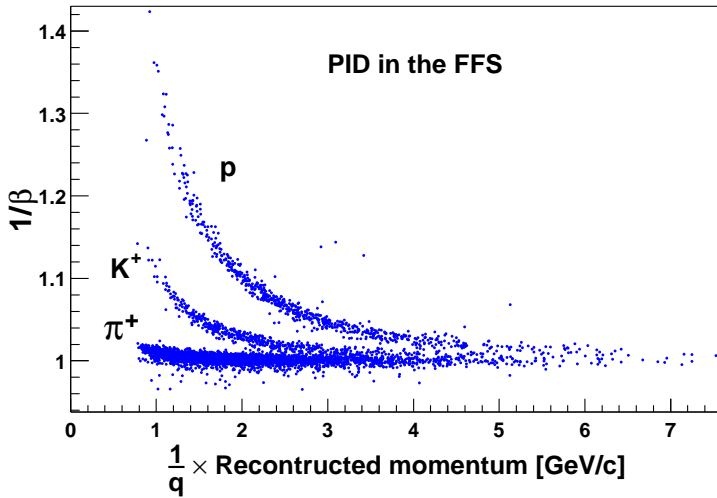


Fig. 9. Particle identification in the FFS.

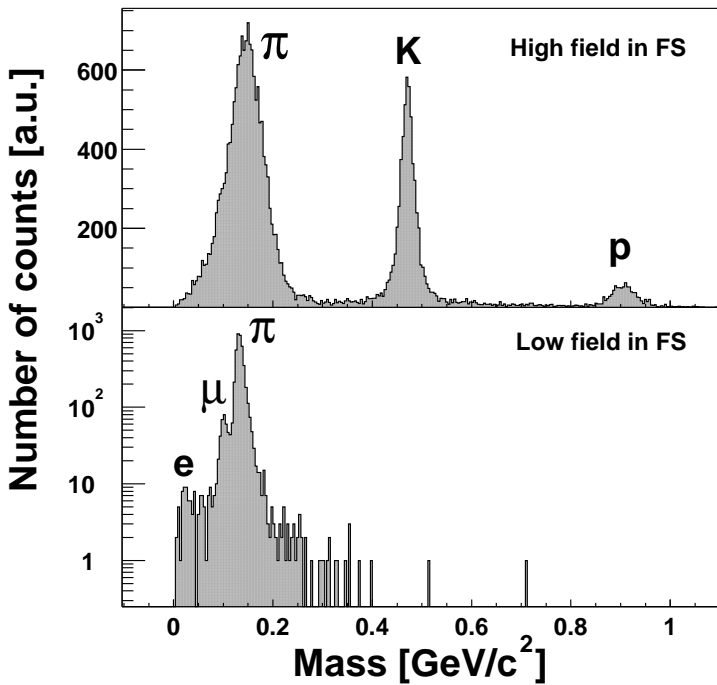


Fig. 10. Mass distribution of particles identified by the RICH detector. The low field data (bottom panel) and the high field data (top panel) particle's momenta ranging from 3 to 6 GeV/c and 8 to 20 GeV/c, respectively.

4.2. Results

The particle yield in the FS, in the low momentum, is determined by selecting tracks having a TOF within a $\pm 2\sigma$ band of the expected TOF *vs* momentum for a given particle type. For higher momentum, above the threshold of the RICH detector the yields can be determined by applying cuts in the m^2 spectra. In the case of MRS, for the results presented here, both methods of the particle yield determination were applied.

Figure 11 shows the dependence of the measured $N(\bar{p})/N(p)$ ratios on collision centrality and on particle momentum for Au + Au collisions at $\sqrt{s_{NN}} = 130$ GeV. The ratios have been corrected for losses of anti-protons due to annihilation evaluated by GEANT simulation to be less than 2% in the MRS and about 3.5% in FS. Figure 11 (left panel) shows the centrality dependence for data summed over all momentum bins, while figure 11 (right panel) shows the p_T dependence for data summed over all centrality bins. It is seen that the centrality and p_T dependence of the ratio is small for the three considered rapidities. The $N(\pi^-)/N(\pi^+)$ ratios (not shown) exhibit a similar lack of centrality and p_T dependence.

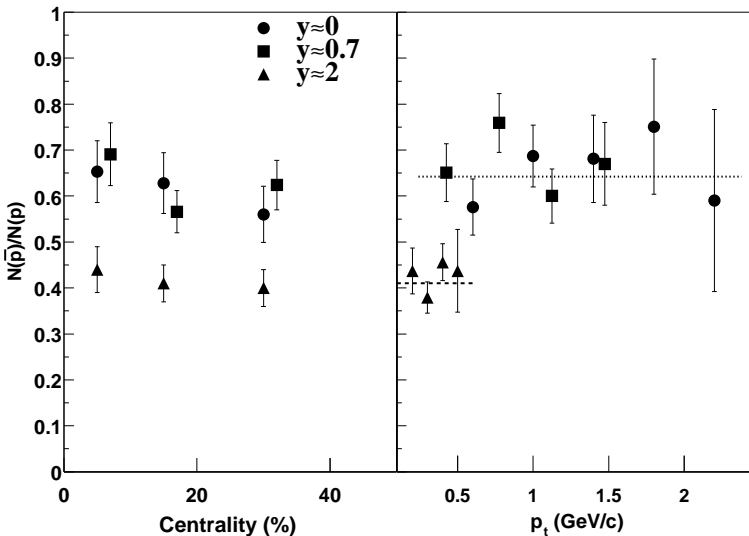


Fig. 11. The left panel shows the centrality dependence of the $N(\bar{p})/N(p)$ ratios for the three rapidity values: $y \approx 0$ (filled circles), $y \approx 0.7$ (open squares) and $y \approx 2$ (filled triangles). Only statistical errors are shown. The data points for $y \approx 0.7$ are shifted slightly for display purpose. The centrality percentages are described in the text. The right panel shows the transverse momentum dependence of the measured $N(\bar{p})/N(p)$ ratio for the same three rapidity intervals for events selected from the 0–40% centrality cut.

The ratios presented in this proceedings have not been corrected for protons and anti-protons that originate from weak decays of hyperons (Λ , Σ , *etc.*). However, making a reasonable assumption about the relative production ratios and primary baryons we found that the correction to the quoted ratios is less than $\pm 5\%$ [24].

Figure 12 presents the anti-particle to particle ratios for pions, kaons and protons as a function of p_T , but here we plot the data for the maximum RHIC energy. For the all measured particle species, both at $y \approx 0$ (top panel) and $y \approx 2$ (bottom panel), the picture displays no evidence of p_T dependence, within the p_T range covered.

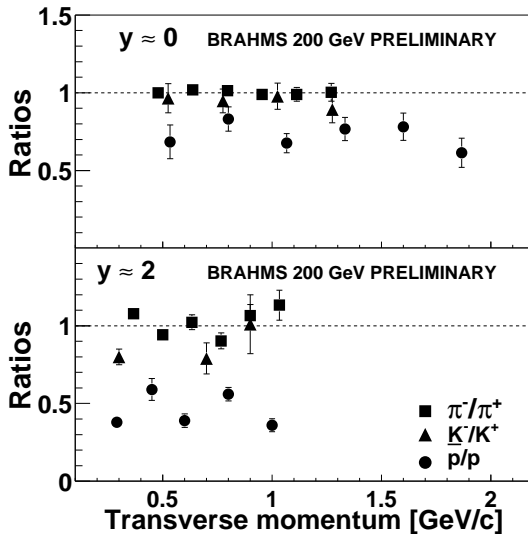


Fig. 12. Anti-particle particle ratios *versus* p_T , for $y \approx 0$ (top panel) and $y \approx 2$ (bottom panel) (see text for more details).

In figure 13 we plot the mid-rapidity anti-particle to particle ratios *versus* the reaction centrality, for three different centrality bins for the 20% most central events. The plotted data are for $\sqrt{s_{NN}} = 200$ GeV. The picture shows no evidence of centrality dependence within the range of 0–20% reaction centrality.

As in the case of data for $\sqrt{s_{NN}} = 130$ GeV (figure 11), the ratios presented in figures 12 and 13 have been summed over all centrality and momentum bins, respectively.

The summary of the rapidity dependence of the measured ratios is presented in figure 14. The top, middle and bottom panel show data for π^-/π^+ , K^-/K^+ , \bar{p}/p , respectively, for $\sqrt{s_{NN}} = 200$ GeV (filled symbols) and for $\sqrt{s_{NN}} = 130$ GeV (open symbols). Only statistical error bars are shown. It

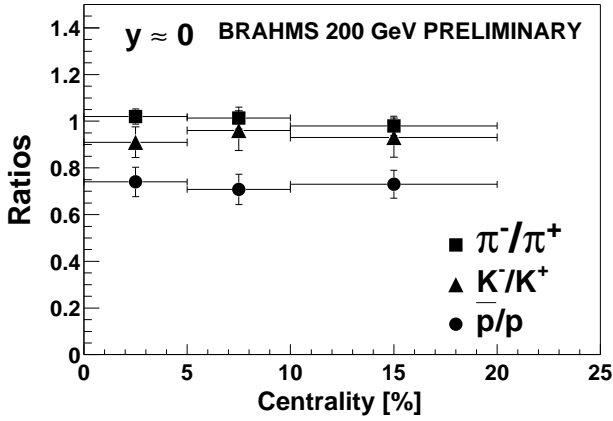


Fig. 13. Anti-particle to particle ratios versus collision centrality.

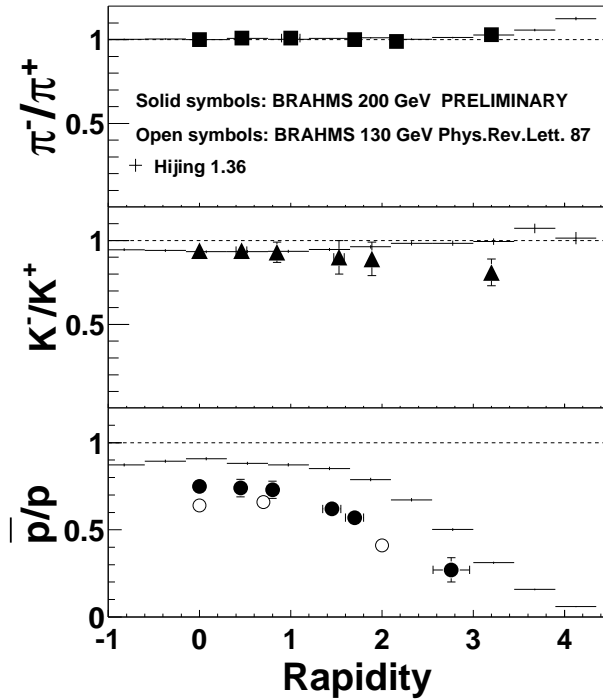


Fig. 14. Anti-particle to particle ratios as a function of rapidity for π^-/π^+ (top panel), K^-/K^+ (middle panel), \bar{p}/p (bottom panel). The crosses are the corresponding ratio predicted by HIJING model. The open symbols from the bottom panel refer to the data at $\sqrt{s_{NN}} = 130$ GeV. The horizontal errors show the rapidity interval covered, and the vertical error are the statistical only.

is seen from the figure that, while the pion ratio is independent of rapidity and consistent with unity, for both RHIC energies, the anti-proton to proton ratio drops significantly with increasing rapidity from $0.64 \pm 0.04(\text{stat}) \pm 0.06$ at $y \approx 0$ to $0.41 \pm 0.04(\text{stat}) \pm 0.06$ at $y \approx 2$ ($\sqrt{s_{NN}} = 130$ GeV), and from $0.75 \pm 0.03(\text{stat}) \pm 0.05$ at $y \approx 0$ to $0.3 \pm 0.04(\text{stat}) \pm 0.06$ at $y \approx 2.8$ ($\sqrt{s_{NN}} = 200$ GeV). The \bar{p}/p ratios do not fall rapidly in the first unit of rapidity, which may indicate that in this rapidity region the chemical equilibrium is achieved, for both energies studied. The K^-/K^+ is on average very close to unity, and therefore, is the highest value so far observed in the heavy ion collision.

5. Results *versus* models

Finally, let us make a look on how the various models available on the market, are consistent with the data already presented. Figure 15 compares the measured ratios (left side), and particle densities (right side), to calculations using the HIJING model [17], the FRITIOF 7.02 [25] string model and the UrQMD cascade model [26], using the same cuts on centrality and transverse momentum as those applied in the data analysis. All data and calculations discussed here refer to Au + Au reaction at $\sqrt{s_{NN}} = 130$ GeV.

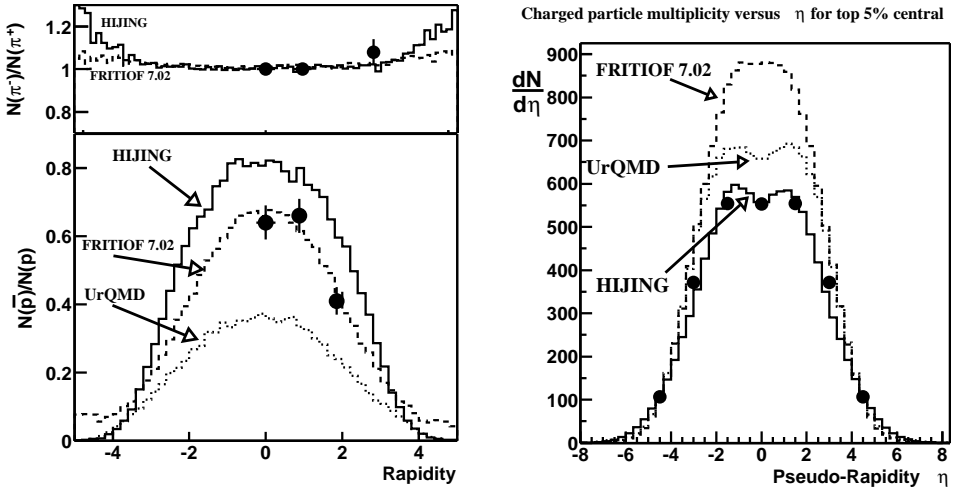


Fig. 15. Comparison of the measured $N(\bar{p})/N(p)$ (lower panel) and $N(\pi^-)/N(\pi^+)$ (upper panel) ratios to model predictions. The data shown are for 0–40% of central events and integrated over the transverse momentum range shown in figure 11. The three model calculations (HIJING, FRITIOF, and UrQMD) are shown for comparison. See text for details.

All three models reproduce the observed pion ratios well. The FRITIOF model reproduces the anti-protons/protons ratios quite well, but it overpredicts by $\approx 30\%$ the charged particles yield at $\eta \approx 0$. This is mainly related to a fairly large degree of baryonic stopping predicted by the model. On the other hand the HIJING model, which describes the overall charge particle yields well, fails in describing the anti-proton to proton ratios. This feature of the model is in turn related to a small stopping of the projectile baryons. UrQMD, which is not partonic model, fails both in describing anti-proton/proton ratio (by almost a factor of 2) and in describing the charged particle multiplicity which supports the importance of the partonic degree of freedom in description of the nucleus–nucleus collisions at the RHIC energies.

These models exemplify the present theoretical understanding of the heavy ion collisions in this new energy regime. None of the models offers a consistent description of the observed features.

6. Summary

In summary, the BRAHMS experiment have measured pseudorapidity densities and anti-particle to particle ratios of charged particles produced in Au + Au collisions at $\sqrt{s_{NN}} = 130$ GeV and at $\sqrt{s_{NN}} = 200$ GeV.

We found that the charged particle production increases by a constant amount from $\sqrt{s_{NN}}=130$ GeV to $\sqrt{s_{NN}}=200$ GeV in a wide region around mid-rapidity. The data are well reproduced by calculations based on high-density QCD and by the AMPT/HIJING microscopic parton model. A phenomenological analysis in terms of a superposition of soft- and hard-scattering particle production indicates that the hard-scattering component seen at mid-rapidity for central collisions, at $\sqrt{s_{NN}}=200$ GeV, is not significantly enhanced as compared to $\sqrt{s_{NN}}=130$ GeV results. We find good consistency with the gluon saturation model of Kharzeev and Levin, but stress that within errors of models and data alike, the data can be equally well reproduced by other models that do not require parton-collision saturation.

Regarding the anti-particle to particle ratios we found, that the pion ratio is close to unity, as would be expected at these bombarding energies, where around 4000 charged particles (predominantly pions) are produced in central collision. The ratio of anti-proton to proton at mid-rapidity increases from 0.64 at $\sqrt{s_{NN}}=130$ GeV [8, 20, 24] to 0.75 at $\sqrt{s_{NN}}=200$ GeV and is still below unity and decreases towards forward rapidity. However, the decrease is very weak (if any) within the ± 1 unit around the central rapidity that may indicate that in this rapidity range the chemical balance is reached. The anti-proton to proton ratio rapidity dependence serves as

an indicator of the interplay between the baryon transport to mid-rapidity and anti-baryon and baryon pair production. To fully answer the questions regarding the issues of transparency and stopping we will supplement the presented particle ratios with the measurements of the net-bayron density, however, the current results suggest that there is still a significant contribution from participant baryons over the entire rapidity range and that the full transparency of the Bjorken limit has not yet been reached.

Finally, we may also conclude that, at the present time, none of the models offer a fully consistent description of the observed reaction features for collisions in this new energy domain.

We thank the RHIC collider team for their efforts. This work was supported by the Division of Nuclear Physics of the U.S. Department of Energy, the Danish Natural Science Research Council, the Korea Research Foundation, the Research Council of Norway, the Polish State Committee for Scientific Research (KBN) and the Romanian Ministry of Research.

REFERENCES

- [1] Xin-Nian Wang, M. Gyulassy, *Phys. Rev. Lett.* **86**, 3496 (2001).
- [2] K.J. Eskola, K. Kajantie, K. Tuominen, *Phys. Lett.* **B497**, 39 (2001).
- [3] I.G. Bearden *et al.* (NA44), submitted to *Phys. Rev. C* (2002), `nuc1-ex/0202019`.
- [4] F. Videbæk, O. Hansen, *Phys. Rev.* **C52**, 2684 (1995).
- [5] J.D. Bjorken, *Phys. Rev.* **D27**, 140 (1983).
- [6] M. Adamczyk *et al.* (BRAHMS Collaboration), submitted to *Nucl. Instrum. Methods Phys. Res.* (2002).
- [7] I.G. Bearden *et al.*, *Phys. Lett.* **B523**, 227 (2001).
- [8] C. Adler *et al.*, *Nucl. Instrum. Methods Phys. Res.* **A470**, 488 (2001).
- [9] R.J. Glauber, G. Matthiae, *Nucl. Phys.* **B21**, 135 (1970).
- [10] A. Białas, M. Bleszyński, W. Czyż, *Nucl. Phys.* **B111**, 461 (1976).
- [11] P. Deines-Jones *et al.*, *Phys. Rev.* **C62**, 014903 (2000).
- [12] I.G. Bearden *et al.* (BRAHMS Collaboration), submitted to *Phys. Rev. Lett.* (2001), `nuc1-ex/0112001`.
- [13] D. Kharzeev, E. Levin, *Phys. Lett.* **B523**, 79 (2001); D. Kharzeev, private communication.
- [14] Bin Zhang, C.M. Ko, Bao-An Li, Zi-wei Lin, *Phys. Rev.* **C61**, 067901 (2001).
- [15] Zi-wei Lin, S. Pal, C.M. Ko, Bao-An Li, Bin Zhang, *Phys. Rev.* **C64**, 011902R (2001).
- [16] G.J. Alner *et al.*, *Z. Phys.* **C33**, 1 (1986).

- [17] X.N. Wang, M. Gyulassy, *Phys. Rev.* **D44**, 3501 (1991).
- [18] F. Karsch, [hep-lat/0106019](#).
- [19] K. Adcox *et al.*, *Phys. Rev. Lett.* **86**, 3500 (2001).
- [20] B. Back *et al.* (PHOBOS Collaboration), *Phys. Rev. Lett.* **85**, 3100 (2000).
- [21] C. Adler *et al.* (STAR Collaboration), *Phys. Rev. Lett.* **87**, 112303 (2001).
- [22] D. Kharzeev, M. Nardi, *Phys. Lett.* **B507**, 121 (2001).
- [23] N. Herrmann, J.P. Wessels, T. Wienold, *Annu. Rev. Nucl. Part. Sci.* **49**, 581 (1999).
- [24] I.G. Bearden *et al.* (BRAHMS Collaboration), *Phys. Rev. Lett.* **87**, 112305 (2001).
- [25] B. Anderson *et al.*, *Z. Phys.* **C57**, 485 (1993); H. Pi, *Comput. Phys. Commun.* **71**, 173 (1992).
- [26] S.A. Bass *et al.*, *Prog. Part. Nucl. Phys.* **41**, 225 (1998); M. Bleicher *et al.*, *J. Phys. G. Nucl. Part. Phys.* **25**, 1859 (1999).